A monolithic Lagrangian meshfree scheme for Fluid–Structure Interaction problems within the OTM framework

Jiang Fan[a,c,d], Huming Liao[a], Renjie Ke[b], Erdem Kucukal[b], Umut A. Gurkan[b],
Xiuli Shen[a], Jian Lu[e], Bo Li[b,*]

[a] School of Energy and Power Engineering, Beihang University, Beijing 100191, China
[b] Department of Mechanical and Aerospace Engineering, Case Western Reserve University, Cleveland, OH 44106, USA
[c] Beijing Key Laboratory of Aero-Engine Structure and Strength, Beijing 100191, China
[d] Collaborative Innovation Center of Advanced Aero-Engine, Beijing 100191, China
[e] Guangdong Institute of Aeronautics and Astronautics Equipment & Technology, Zhuhai, Guangdong 519000, China

Highlights

- An incremental variational formulation for Fluid–Structure Interaction (FSI) problems.
- A variational time integration for FSI based on optimal transportation theory.
- A pure Lagrangian description of general fluid and solid flows with viscosity.
- Automatic continuity and force equilibrium on FSI interfaces.
- Monolithic meshfree method for fluid interacting rigid or highly flexible structures.

Abstract

We present a monolithic Lagrangian meshfree solution for Fluid–Structure Interaction (FSI) problems within the Optimal Transportation Meshfree (OTM) framework. The governing equations of the fluid and structure are formulated in the Lagrangian configuration and solved simultaneously in a monolithic way. Mainly, the fully discretized equations are constructed by leveraging on the OTM method to address the challenges in the Lagrangian description of the fluid domain. In this approach, the fluid–structure interface becomes an internal surface of the entire field, and the continuity and force equilibrium on the interface are automatically satisfied without any extra computations. The monolithic Lagrangian solution provides enhanced stability comparing to partitioning approaches and eliminates the problem of free surface and material interface tracking. The presented method enables a Direct Numerical Simulation (DNS) of the fluid flow with the absence of the convective terms. The accuracy and robustness of the OTM FSI approach are systematically investigated by the classical Blasius solution of the boundary layer problem. Furthermore, we illustrate the range and scope of the method through two examples: the impact of a rigid body on the fluid domain in a container and the interaction between the fluid and highly flexible structures in an open channel.

---

* Corresponding author.
 E-mail addresses: fanjiang@buaa.edu.cn (J. Fan), liaohuming@buaa.edu.cn (H. Liao), rxk385@case.edu (R. Ke), exk238@case.edu (E. Kucukal), uxg23@case.edu (U.A. Gurkan), shxl606@buaa.edu.cn (X. Shen), luj@giaaet.com (J. Lu), bxl295@case.edu (B. Li).

1. Introduction

In Fluid–Structure Interaction (FSI) problems, one or more solid structures interact with an internal or surrounding fluid flow. FSI problems play prominent roles in many scientific and engineering fields, yet a comprehensive study of such problems remains a challenge due to their high nonlinearity and multidisciplinary nature [1]. Nevertheless, for most FSI problems, analytical solutions to the model equations are difficult to obtain, and experimental studies are limited by the state-of-the-art diagnostics and usually inefficient and expensive. Alternatively, numerical simulation is an enabling tool to explore the underlying physics in FSI phenomenon for its low cost and high efficiency.

FSI modeling and simulations may be broadly divided into two categories: partitioned approach and monolithic approach. The partitioned approach [2,3] allows solving the flow equations and the structure equations separately with techniques and software developed specifically for each one. For instance, one can use the Eulerian grid-based method, such as Finite Element Method (FEM), Finite Differences (FD) method and Finite Volume (FV) method, or the Smooth Particle Hydrodynamics (SPH) [4,5], to solve the fluid governing equations and a Lagrangian Finite Element solution for the structure. The continuity and equilibrium conditions on the fluid–structure interface may be enforced by directly applying the individual solutions as boundary conditions on each subdomain or by solving additional equilibrium equations. This procedure is done every time step using specific time integration schemes. Consequently, this approach experiences inherent difficulties in obtaining exact momentum and energy conservation properties, which necessitates a stable and accurate coupling algorithm to alleviate instabilities [6,7]. Many studies have analyzed the primary sources of instabilities in the partitioned approach, including the density, geometry and nonlinear material response of the structure [8–11] as well as the matching of the time-integration scheme for the individual solutions of the fluid and solid domains [12]. Another challenge in the partitioned approach comes from the fact that the structure may be highly deformable, in which case the location of the interface is unknown and depends on the time history of both the fluid and the structure domain. Conventional methods for the dynamic tracking of the fluid–structure interfaces include Level Sets [13] and Front Tracking algorithm [14], which are expensive regarding computational cost. Also, there have been several advances for the coupling of the solutions from both parts, for example, the moving reference frames [15] or non-boundary conforming formulations [16,17].

On the other hand, a monolithic modeling allows making no distinction between the fluids and the solids, while each subdomain is considered to have different material properties. A single simulation tool can be used for solving simultaneously both fluid and solids described by one system of equations [18–21], which ensures the exact momentum and energy balance. Monolithic schemes are theoretically more stable and accurate than partitioned methods but computationally more expensive per time step [21]. The conventional monolithic approach uses the Arbitrary Lagrangian–Eulerian formulation (ALE) [22,23]. In the ALE approaches the fluid mesh is allowed to deform matching the deformation of the structural domain. This greatly facilitates the application of the interface boundary conditions and makes ALE-based approaches very attractive (e.g. [24–27]). Similarly, spacetime approaches [28–30] provide an accurate framework for the solution of complex FSI problems. Refs. [31,32] discuss in detail the time integration scheme, the implications related to the strong coupling algorithm and the techniques used for mesh-moving. An interesting work on the application of the ALE approach for monolithic FSI is presented in [33]. There the formulation is based upon the iso-geometric approach in conjunction with a generalized alpha time integration scheme. However, even the most advanced ALE formulations arrive at their limits when the domain shape deformations are large, and remeshing and remapping of state variables are still necessary for large local deformation and unconstrained multiphase flows.

Alternatively, a unified Lagrangian formulation for FSI is proposed in [34] using the Particle Finite Element Method (PFEM) [35,36]. The main advantage of the unified Lagrangian formulation is that the convective terms disappear from the fluid equations. The counterpart is that this may require a lot of remeshing due to mesh entanglements for the fluid flows. The limitation in the grid-based Lagrangian modeling of the fluid can be addressed by the meshfree methods. Recently, Li and Ortiz [37,38] developed an incremental updated Lagrangian meshfree scheme, the Optimal Transportation Meshfree (OTM) method, which is capable of solving general fluid and solid flows, possibly involving multiple phases, viscosity and general inelastic and rate-dependent constitutive relations, arbitrary variable domains with discontinuity and boundary conditions. The OTM method is constructed through an integration of optimal transportation theory [39] with Local Maximum Entropy (LME) meshfree approximation [40] and material point sampling. The optimal-transportation variational framework results in geometrically exact updates of the local volumes and mass densities, thus bypassing the need for solving a costly Poisson equation for the pressure and eliminating the mass conservation errors that afflict Eulerian formulations. Furthermore, by adopting a discrete

Hamilton principle based on a time-discrete action furnished by optimal transportation theory, the discrete trajectories have exact conservation properties including symplecticity, linear and angular momentum. The introduction of material points provides an effective numerical integration rule for the remaining terms of the action and facilitates tracking the complex local constitutive updates. Fields requiring differentiation, such as deformation and temperature gradient, are interpolated from node values using LME meshfree shape functions. The LME shape functions are affine on the boundary, which enables the direct coupling of fluid flows to highly deformable structures. In addition, the LME shape functions have the key property of possessing a weak Kronecker-delta property at the boundary, which overcomes a common difficulty in meshfree methods and enables direct imposition of essential boundary conditions. Moreover, a convenient feature of OTM is that seizing contact is accounted for automatically by simply allowing nodes from different bodies to belong to the local neighborhoods of material points. The ensuing cancellation of linear momentum automatically accounts for dynamic contacts of the seizing type [41]. The combination of these desirable attributes effectively addresses many of the difficulties in the current state-of-the-art approaches, thereby supplying a methodology that is well-suited to the simulation of general, possibly coupled, fluid/solid/structural problems.

In this paper, we will employ a uniform set of governing equations in the Lagrangian description for both the fluid and solid domain [42]. The variational constitutive updates [43] will be used to describe the dynamic response of general fluid and solid flows involving viscous dissipation. The fully discretized governing equations of the whole domain will be formulated within the OTM framework and solved simultaneously, which results in a monolithic Lagrangian meshfree solution of fluid–structure interaction problems. In specific, the inertia term in the variational structure of a rate problem will be discretized explicitly by the optimal transportation theory. In this approach, the fluid–structure interface becomes an internal surface, which automatically ensures the continuity and force equilibrium and leads to a more stable and accurate solution with fast convergence [11]. Additionally, the use of Lagrangian meshfree formulations for the fluid eliminates the problem of free surface and interface tracking and addresses the challenge of the mesh entanglement.

The remainder of this paper is organized as follows. Section 2 introduces the monolithic Lagrangian framework for FSI problems including the governing equations, the uniform constitutive relation and the variational structure with viscous dissipation mechanism for fluid and solid material in Lagrangian configuration. Section 3 illustrates the temporal discretization and spatial discretization of the proposed approach within the OTM framework, and then selected numerical examples of application are presented in Section 4 that demonstrate the scope and versatility of the method. Some concluding remarks are finally collected in Section 5.

2. Monolithic Lagrangian framework for fluid–structure interaction

2.1. Governing equations for fluid and solid materials

Consider a continuous body, which consists of fluid material and solid material, initially occupying a reference configuration $\Omega_0 \subset \mathbb{R}^d$ at $t = 0$ (here and subsequent, the reference configuration refers to the undeformed configuration), and undergoing a motion described by a time-dependent deformation mapping $\boldsymbol{\varphi} : \Omega_0 \times [0, T] \to \mathbb{R}^d$. Material particles in the reference configuration are denoted by $X \in \Omega_0$ mapping to points $\boldsymbol{x} = \boldsymbol{\varphi}(X, t)$ in the deformed configuration $\Omega_t = \boldsymbol{\varphi}(\Omega_0, t)$. Then the motion and deformation of the body is subject to the solution of a general initial boundary value problem in the Lagrangian form, i.e.,

$$\boldsymbol{F}(X, t) = \nabla_0 \boldsymbol{\varphi}(X, t) \qquad \text{in } \Omega_0 \times [0, T], \tag{1}$$

$$\boldsymbol{\varphi}(X, t) = \overline{\boldsymbol{\varphi}}(X, t) \qquad \text{on } \Gamma_u \times [0, T], \tag{2}$$

$$\rho_0 \ddot{\boldsymbol{\varphi}} - \nabla_0 \cdot \boldsymbol{P} = \rho_0 \boldsymbol{B} \qquad \text{in } \Omega_0 \times [0, T], \tag{3}$$

$$\boldsymbol{P} \cdot \boldsymbol{N} = \overline{\boldsymbol{T}} \qquad \text{on } \Gamma_t \times [0, T], \tag{4}$$

$$\boldsymbol{\varphi}(X, 0) = \boldsymbol{\varphi}_0(X) \qquad \text{in } \Omega_0, \tag{5}$$

$$\dot{\boldsymbol{\varphi}}(X, 0) = \boldsymbol{V}_0(X) \qquad \text{in } \Omega_0, \tag{6}$$

$$(\rho \circ \boldsymbol{\varphi}(X, t))J = \rho_0 \qquad \text{in } \Omega_0, \tag{7}$$

where ∇_0 denotes the partial derivatives with respect to X, $\boldsymbol{F}$ is the deformation gradients, $\dot{\boldsymbol{\varphi}}$ and $\ddot{\boldsymbol{\varphi}}$ are the material velocity and acceleration respectively, ρ_0 is the unit mass density in the reference configuration, $\boldsymbol{P}$ is the first Piola–Kirchhoff stress tensor, $\boldsymbol{B}$ is the applied body force per unit mass in the reference configuration, and $J = \det(\boldsymbol{F})$ is

the Jacobian of the deformation. The boundary of domain Ω_0 is $\partial\Omega_0 = \Gamma_u \bigcup \Gamma_t$ and $\Gamma_u \bigcap \Gamma_t = \emptyset$, where Γ_u is the Dirichlet boundary and prescribed the displacement boundary conditions $\overline{\boldsymbol{\varphi}}$, and $\overline{\boldsymbol{T}}$ is the external forces along the Neumann boundary Γ_t. The Cauchy stress tensor follows from $\boldsymbol{P}$ in the form

$$\boldsymbol{\sigma} = J^{-1}\boldsymbol{P}\boldsymbol{F}^T. \tag{8}$$

We will employ this uniform set of governing equations in the Lagrangian description for both the fluid and solid domain. In subsequent sections, those equations are taken as the basis for formulating constitutive relations, the weak form and variational structure for FSI problems.

2.2. Uniform constitutive framework for fluid and solid materials

In addition to the uniform set of governing equations, we require a uniform constitutive framework within which to describe the fluid and solid materials. To this end, we adopt a standard constitutive update algorithm proposed by Radovitzky and Ortiz [43]. Assume the existence of a Helmholtz free energy density $A(\boldsymbol{F})$ per unit undeformed volume. For simplicity, we restrict attention to isothermal processes and omit the dependence of A and all other state functions on temperature. Thus the first Piola–Kirchhoff stress tensor $\boldsymbol{P}$ can be decomposed additively,

$$\boldsymbol{P} = \boldsymbol{P}^e + \boldsymbol{P}^v, \tag{9}$$

into an equilibrium part $\boldsymbol{P}^e$ and a viscous part $\boldsymbol{P}^v$. The equilibrium stress $\boldsymbol{P}^e$ follows from Coleman's relations as

$$\boldsymbol{P}^e = \frac{\partial A(\boldsymbol{F})}{\partial \boldsymbol{F}}. \tag{10}$$

from a potential if there exists a function $\Phi^*(\dot{\boldsymbol{F}})$ which denotes the viscous dissipation. Thus, the viscous part $\boldsymbol{P}^v$ of the stresses follow in the form

$$\boldsymbol{P}^v(\dot{\boldsymbol{F}}; \boldsymbol{F}) = \frac{\partial \Phi^*(\dot{\boldsymbol{F}})}{\partial \dot{\boldsymbol{F}}}. \tag{11}$$

For elastic solid

$$\boldsymbol{P}^v = \boldsymbol{0}, \quad \boldsymbol{P} = \boldsymbol{P}^e. \tag{12}$$

For compressible Newtonian fluid, the viscous dissipation $\Phi^*(\dot{\boldsymbol{F}})$ takes a form,

$$\Phi^*(\dot{\boldsymbol{F}}) = \mu J \boldsymbol{d}^{\text{dev}} : \boldsymbol{d}^{\text{dev}}, \tag{13}$$

$$\boldsymbol{d}^{\text{dev}} = \boldsymbol{d} - \frac{1}{3}\text{tr}(\boldsymbol{d})\boldsymbol{I}, \tag{14}$$

$$\boldsymbol{d} = \text{sym}(\dot{\boldsymbol{F}}\boldsymbol{F}^{-1}), \tag{15}$$

where $\boldsymbol{d}$ is the rate of deformation tensor, $\boldsymbol{d}^{\text{dev}}$ is its deviatoric component. The viscous stress is given by

$$\boldsymbol{P}^v(\dot{\boldsymbol{F}}; \boldsymbol{F}) = \frac{\partial \Phi^*(\dot{\boldsymbol{F}})}{\partial \dot{\boldsymbol{F}}} = J\boldsymbol{\sigma}^v\boldsymbol{F}^{-T}, \tag{16}$$

where

$$\boldsymbol{\sigma}^v = 2\mu\boldsymbol{d}^{\text{dev}}, \tag{17}$$

is the viscous part of the Cauchy stress tensor, and μ denotes the shear viscosity coefficient. Furthermore, the free energy density A is represented by the equation of state, which leads to the equilibrium stress $\boldsymbol{P}^e$ as

$$\boldsymbol{P}^e(\boldsymbol{F}) = \frac{\partial A(J)}{\partial \boldsymbol{F}} = Jp(J)\boldsymbol{F}^{-T}, \tag{18}$$

where

$$p(J) = \frac{\partial A(J)}{\partial J}, \tag{19}$$

is the equilibrium pressure. For instance, the Tait–Murnaghan equation of state, $p(J) = p_0 + \frac{K}{n}(J^{-n} - 1)$, is often employed to describe the volumetric responses of water [44]. Therefore, the first Piola–Kirchhoff stress tensor $\boldsymbol{P}$ for compressible Newtonian fluid can be obtained as

$$\boldsymbol{P} = \boldsymbol{P}^e + \boldsymbol{P}^v = J \left(p(J)\boldsymbol{I} + 2\mu \boldsymbol{d}^{\text{dev}} \right) \boldsymbol{F}^{-T} \tag{20}$$

which is consistent with the Cauchy stress tensor of compressible Newtonian fluid in the Eulerian configuration. It is noteworthy that this framework is general enough to model fluid and solid flows with arbitrary constitutive relations as long as the Helmholtz free energy density and dissipation potential are defined.

3. Optimal transportation meshfree implementation

In this section, we proceed to establish a fully discretized version of the governing equations (1)–(7) in space and time by adopting the Optimal Transportation Meshfree (OTM) framework. The OTM method is originally introduced by Li and Ortiz [37], which is constructed through an integration of optimal transportation theory [39] for time discretization with Local Maximum Entropy (LME) meshfree approximation [40] and material point sampling.

3.1. Incremental variational formulation

In order to formulate the time-discretized governing equations, we will extend the variational updates proposed by Ortiz and Stainier 1999 [45] for general dissipative systems to account for the inertia terms. To this end, the corresponding action $I[\dot{\boldsymbol{\varphi}}]$ of general fluid–structure interaction problems with viscosity follows from the formula

$$I[\dot{\boldsymbol{\varphi}}] = \int_{\Omega_{FSI}} \left(\dot{K} + \dot{A}(\boldsymbol{F}) + \Phi^*(\dot{\boldsymbol{F}}) - \rho_0 \boldsymbol{B} \cdot \dot{\boldsymbol{\varphi}} \right) dV - \int_{\Gamma_t} \overline{\boldsymbol{T}} \cdot \dot{\boldsymbol{\varphi}} dS \tag{21}$$

where $\dot{()}$ denotes the material time derivative and $\Omega_{FSI} = \Omega_f \bigcup \Omega_s$ is the union of the fluid and solid subdomains, Ω_f and Ω_s. K, A and Φ^* are the kinetic energy, Helmholtz free energy density and a dissipation pseudo-potential function which represents the viscous response of the material, respectively [42,45]. The fluid flow will be considered as compressible or near incompressible material in our formulation.

The functional given in Eq. (21) shows the variational characterization of a rate problem, i.e., the problem of finding the rate of change of the state variables given its current state and boundary conditions. In calculations, it is necessary to establish the time discretization of the variational formulation. Thus the time-dependent problem can be reduced to a sequence of incremental problems each characterized by a minimum principle. Formally, the time-discretized incremental variational problem can be derived by recourse to minimizing paths [46], leading to the definition of an equivalent static problem. On the other hand, it is also sufficient to identify any convenient incremental potential over a time interval which is consistent with the field equations. The essential difficulty for a dynamic problem is to directly embed a specific time discretization of the inertia terms within the incremental variational formulation. However, Benamou and Brenier [47,48] showed that the so called L^2 Kantorovich (or Wasserstein) distance between the initial and final mass densities in $[t_k, t_{k+1}]$ gives the exact minimum of the action of the incremental kinetic energy in fluids, i.e.,

$$d_W^2(\rho_k, \rho_{k+1}) = \inf_{\text{paths}} \left\{ (t_{k+1} - t_k) \int_{t_k}^{t_{k+1}} \int_{\Omega_k} \rho_k |\dot{\boldsymbol{\varphi}}|^2 dV dt \right\}, \tag{22}$$

where the L^2 Kantorovich distance is defined as

$$d_W^2(\rho_k, \rho_{k+1}) = \inf_T \int_{\Omega_k} |T(\boldsymbol{x}) - \boldsymbol{x}|^2 \rho_k(\boldsymbol{x}) dV, \tag{23}$$

and T is any admissible map transporting ρ_k to ρ_{k+1}. The mass densities are related by the Jacobian equation

$$(\rho \circ T)(\boldsymbol{x}, t) \det(\nabla T) = \rho_k(\boldsymbol{x}) \quad \text{for } t \in [t_k, t_{k+1}]. \tag{24}$$

Li and Ortiz employed the Wasserstein distance for the discrete kinetic energy of general fluid and solid flows in the OTM method, and generalized the Benamou–Brenier differential formulation of optimal mass transportation problems to problems including arbitrary geometries and constitutive behavior [37]. In this work, we will adopt the time-discretized inertia terms using the Wasserstein distance to address the challenge in the variational incremental

formulation of rate problems. To this end, let $t_0 = a < t_1 < \cdots < t_k < t_{k+1} < \cdots < t_{n-1} < t_n = b$ be a discretization of the time interval $[a, b]$ and assume that the state $(\rho_k, \boldsymbol{\varphi}_k)$ at time t_k is known. Then, we wish to consistently approximate the state $\boldsymbol{\varphi}_{k+1}$ at time t_{k+1} as the solution of an extremum problem. By a consistent approximation we mean that the limits of the divided differences $(\boldsymbol{\varphi}_{k+1} - \boldsymbol{\varphi}_k)/\Delta t$ as $\Delta t = t_{k+1} - t_k$ tends to zero satisfy the rate field equations. Introduce the incremental functional

$$I_k[\boldsymbol{\varphi}_{k+1}] = \inf_{\text{paths}} \int_{t_k}^{t_{k+1}} I[\dot{\boldsymbol{\varphi}}]dt. \tag{25}$$

Thus, we can define the semi-discretized incremental functional with the aid of Eq. (22) as

$$I_k[\boldsymbol{\varphi}_{k+1}] = \frac{1}{2} \frac{\mathrm{d}_W^2(\rho_k, \rho_{k+1})}{\Delta t} + \int_{\Omega_{FSI}} \left(A_{k+1} - A_k + \Delta t \, \Phi^*(\frac{\boldsymbol{F}_{k+1} - \boldsymbol{F}_k}{\Delta t}) \right) dV$$
$$- \int_{\Omega_{FSI}} \rho_k \boldsymbol{B}_{k+1} \cdot (\boldsymbol{\varphi}_{k+1} - \boldsymbol{\varphi}_k)dV - \int_{\Gamma_t} \overline{\boldsymbol{T}}_{k+1} \cdot (\boldsymbol{\varphi}_{k+1} - \boldsymbol{\varphi}_k)dS \tag{26}$$

where the subscript k signifies that $I_k[\boldsymbol{\varphi}_{k+1}]$ depends parametrically on the initial state $\boldsymbol{\varphi}_k$ at t_k, and the minimum is taken over all admissible paths joining $\boldsymbol{\varphi}_k$ at time t_k to $\boldsymbol{\varphi}_{k+1}$ at time t_{k+1}. Taking variations (Ref. [39], Theorem 8.13) gives

$$\delta I_k = \int_{\Omega_{FSI}} \frac{2\rho_k}{t_{k+1} - t_{k-1}} \left(\frac{\boldsymbol{\varphi}_{k\to k+1}(\boldsymbol{x}) - \boldsymbol{x}}{t_{k+1} - t_k} + \frac{\boldsymbol{\varphi}_{k-1\to k}^{-1}(\boldsymbol{x}) - \boldsymbol{x}}{t_k - t_{k-1}} \right) \cdot \delta\boldsymbol{\varphi}_{k+1}dV$$
$$+ \int_{\Omega_{FSI}} (\boldsymbol{P}_{k+1}^e + \boldsymbol{P}_{k+1}^v) : \delta\boldsymbol{F}_{k+1}dV \tag{27}$$
$$- \int_{\Omega_{FSI}} \rho_k \boldsymbol{B}_{k+1} \cdot \delta\boldsymbol{\varphi}_{k+1}dV - \int_{\Gamma_t} \overline{\boldsymbol{T}}_{k+1} \cdot \delta\boldsymbol{\varphi}_{k+1}dS,$$

where the minimizer of the incremental action in $[t_k, t_{k+1}]$ is given in terms of McCann's displacement interpolation [49],

$$\boldsymbol{\varphi}(\boldsymbol{x}, t) = \frac{t_{k+1} - t}{t_{k+1} - t_k}\boldsymbol{x} + \frac{t - t_k}{t_{k+1} - t_k}\boldsymbol{\varphi}_{k\to k+1}(\boldsymbol{x}), \tag{28}$$

and

$$\dot{\boldsymbol{\varphi}}(\boldsymbol{x}, t) = \frac{\boldsymbol{\varphi}_{k\to k+1}(\boldsymbol{x}) - \boldsymbol{x}}{t_{k+1} - t_k}. \tag{29}$$

Enforcing stationarity, i.e., $\delta I_k = 0$, yields the linear momentum conservation and boundary conditions in the interval $[t_k, t_{k+1}]$. The discrete motion consists of incremental transference maps $\boldsymbol{\varphi}_{k\to k+1}$ transporting ρ_k into ρ_{k+1} optimally with respect to the cost function (23).

3.2. Spatial discretization

Next, we proceed to the spatial discretization of the variations of the semi-discrete action (Eq. (27)). In general, solving the fluid flow using Lagrangian grid-based methods is cumbersome due to the mesh entanglements and needs for frequent remeshing. Therefore, we will utilize the OTM discretization scheme for the entire computational domain, where all the field information is carried by two sets of points, namely nodes and material points, as shown in Fig. 1. In specific, the nodes $\boldsymbol{x}_{a,k}$ carry position information, such as displacement, velocity, and acceleration, while the local state of materials is evaluated at the material points $\boldsymbol{x}_{p,k}$, for instance, the local strain, stress, and internal variables, etc. The material points serve as integration points as well, which supplies a convenient way for numerical integration. Analogue to the Finite Element Method, we set the initial position of the material points and nodes using a conforming mesh for Ω_{FSI}, where the nodes of the finite element mesh become the nodes in the OTM method and the quadrature points of the finite elements are considered as the OTM material points. The connectivity between the material points and nodes are initialized using the connectivity of the finite element mesh but dynamically reconstructed during the computation by using a search algorithm based on the deformation-dependent geometrical information.
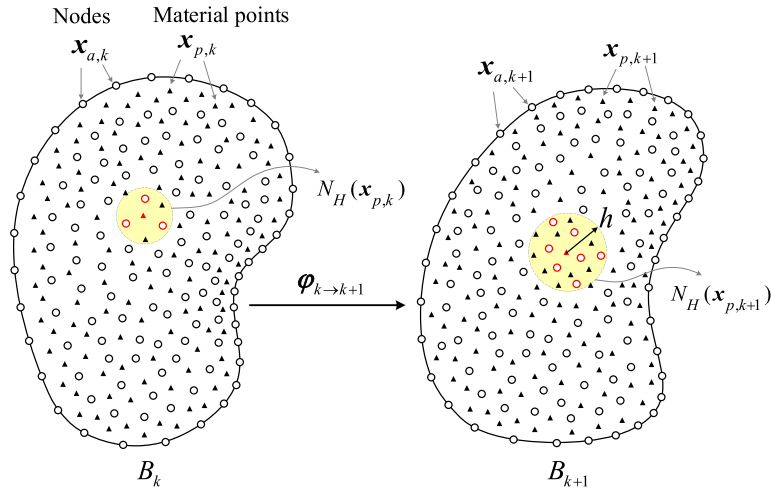
Fig. 1. Schematic of the OTM approximation scheme, showing two successive configurations Ω_k and Ω_{k+1} of the body, mapped into each other by the incremental deformation mapping $\boldsymbol{\varphi}_{k\rightarrow k+1}$ and the corresponding sets of nodes $\boldsymbol{x}_{a,k}$ and $\boldsymbol{x}_{a,k+1}$, and material points $\boldsymbol{x}_{p,k}$ and $\boldsymbol{x}_{p,k+1}$, respectively. $N_H(\boldsymbol{x}_{p,k})$ represents the neighborhood of material point $\boldsymbol{x}_p$ at t_k, and $N_H(\boldsymbol{x}_{p,k+1})$ stands for the neighborhood of material point $\boldsymbol{x}_p$ at t_{k+1}, and h is the scope of the neighborhood of $\boldsymbol{x}_{p,k+1}$. The nodes included in the neighborhood will be used for approximation calculations.

We consider the standard Ritz–Galerkin approach to approximate the displacement using Local Maximum Entropy (LME) msehfree shape functions, i.e.,

$$\boldsymbol{\varphi}(X, t) = \sum_{a=1}^{N} \boldsymbol{X}_{a,t} N_a(X), \tag{30}$$

$$\delta\boldsymbol{\varphi}(X, t) = \sum_{a=1}^{N} \delta\boldsymbol{X}_{a,t} N_a(X), \tag{31}$$

where $\boldsymbol{\varphi}(X, t)$ is the position of an arbitrarily unknown point X at time t, N signifies the total number of the nodes of the whole domain, $N_a(X)$ is the shape function of the node X_a, and $\boldsymbol{X}_{a,t}$ is the position of node X_a at time t. Consequently, the transference maps $\boldsymbol{\varphi}_{k\rightarrow k+1}$ must be approximated by conforming interpolations of the form

$$\boldsymbol{\varphi}_{k\rightarrow k+1}(\boldsymbol{x}) = \sum_{a\in N_H(\boldsymbol{x})} \boldsymbol{x}_{a,k+1} N_a(\boldsymbol{x}) \tag{32}$$

and the position of the material points at time t_{k+1} as well as the deformation gradient are approximated from the node degrees of freedom as

$$\boldsymbol{x}_{p,k+1} = \sum_{a\in N_H(\boldsymbol{x}_{p,k})} \boldsymbol{x}_{a,k+1} N_a(\boldsymbol{x}_{p,k}), \tag{33}$$

and

$$\boldsymbol{F}_{p,k+1} = \nabla\boldsymbol{\varphi}_{k\rightarrow k+1}(\boldsymbol{x}_{p,k})\boldsymbol{F}_{p,k}, \tag{34}$$

where $N_H(\boldsymbol{x}_{p,k})$ represents the neighborhood of a material point $\boldsymbol{x}_p$ at t_k as Fig. 1 shown.

For completeness, we briefly summarize the construction of the LME shape functions as introduced in [40]. Let $\Omega_{Max-Ent}$ be the convex hull of the node set at t_k, and the shape function of the node $\boldsymbol{x}_{a,k}$ at a given material point $\boldsymbol{x}_{p,k}$

is defined as the solution of problem (35):

$$\text{minimize} \quad f_\beta \equiv \beta \sum_{a=1}^{M} N_a(\boldsymbol{x}_{p,k})|\boldsymbol{x}_{p,k} - \boldsymbol{x}_{a,k}|^2 + \sum_{a=1}^{M} N_a(\boldsymbol{x}_{p,k}) \log N_a(\boldsymbol{x}_{p,k}),$$

$$\text{subject to:} \quad N_a(\boldsymbol{x}) \geqslant 0, \ a \in [1, M], \tag{35}$$

$$\sum N_a(\boldsymbol{x}) = 1,$$

$$\sum N_a(\boldsymbol{x})\boldsymbol{x}_a = \boldsymbol{x},$$

where $\beta \in \mathbb{R}^+$ is a Pareto optimal parameter used to ponder the locality term against the entropy term in the objective function.

The constraints in the minimization problem ensure that the resulting shape functions satisfy the zeroth and first order consistency. The solution of the minimization problem is unique and can be directly calculated as:

$$N_a(\boldsymbol{x}) = \frac{1}{Z(\boldsymbol{x}, \boldsymbol{\lambda}^*(\boldsymbol{x}))} \exp\left[-\beta|\boldsymbol{x} - \boldsymbol{x}_a|^2 + \boldsymbol{\lambda}^*(\boldsymbol{x}) \cdot (\boldsymbol{x} - \boldsymbol{x}_a)\right], \tag{36}$$

where:

$$\boldsymbol{\lambda}^*(\boldsymbol{x}) = \arg \min_{\boldsymbol{\lambda} \in \mathbb{R}^n} \log Z(\boldsymbol{x}, \boldsymbol{\lambda}), \tag{37}$$

$$Z(\boldsymbol{x}, \boldsymbol{\lambda}) = \sum_{a=1}^{M} \exp\left[-\beta|\boldsymbol{x} - \boldsymbol{x}_a|^2 + \boldsymbol{\lambda} \cdot (\boldsymbol{x} - \boldsymbol{x}_a)\right]. \tag{38}$$

It is noteworthy that the original constrained minimization problem (35) is replaced by finding the minimizer $\boldsymbol{\lambda}^*$ of a scalar function defined in $\mathbb{R}^n$, where n is the spatial dimension of the computational domain, in the calculation of the meshfree shape functions. This unconstrained minimization problem with convexity can be solved very efficiently and robustly by a combination of Newton–Raphson and Nelder–Mead simplex algorithms. Furthermore, unlike other optimization-based meshfree approximation schemes, such as Moving Least Square (MLS), the computational cost of LME shape functions is independent on the number of nodes in the neighborhood, which furnishes an effective means of solving extremely large deformation problems. In practice, a dimensionless parameter γ related to β by $\gamma = \beta h^2$ is used to control the support width of the shape functions. Fig. 2 shows the LME shape functions with different values of γ and the definition of local characteristic length h in a two-dimensional convex domain.

Finally, variations of semi-discrete incremental potential δI_k (Eq. (27)) are now taken with respect to nodal unknowns and stationarity conditions yield fully-discrete mechanical balance equations, which can alternatively be written

$$m_{a,k+1}\ddot{\boldsymbol{\varphi}}_{a,k+1} = \boldsymbol{f}_{a,k+1}^{\text{ext}} - \boldsymbol{f}_{a,k+1}^{\text{int}}, \tag{39}$$

where $m_{a,k+1}$ denotes the lumped mass of the node $\boldsymbol{x}_a$ at t_{k+1},

$$\ddot{\boldsymbol{\varphi}}_{a,k+1} = \frac{2}{t_{k+1} - t_{k-1}}\left(\frac{\boldsymbol{x}_{a,k+1} - \boldsymbol{x}_{a,k}}{t_{k+1} - t_k} - \frac{\boldsymbol{x}_{a,k} - \boldsymbol{x}_{a,k-1}}{t_k - t_{k-1}}\right) \tag{40}$$

is a central difference approximation of the nodal acceleration. Thus, update of the nodal coordinates is obtained as

$$\boldsymbol{x}_{a,k+1} = \boldsymbol{x}_{a,k} + (t_{k+1} - t_k)\boldsymbol{m}_{a,k+1}^{-1}\left(\boldsymbol{l}_{a,k} + \frac{t_{k+1} - t_{k-1}}{2}(\boldsymbol{f}_{a,k+1}^{\text{ext}} - \boldsymbol{f}_{a,k+1}^{\text{int}})\right) \tag{41}$$

where the linear momenta at t_k is given by

$$\boldsymbol{l}_{a,k} = m_{a,k+1}\frac{\boldsymbol{x}_{a,k} - \boldsymbol{x}_{a,k-1}}{t_k - t_{k-1}} \tag{42}$$

The internal nodal forces $\boldsymbol{f}_{a,k+1}^{\text{int}}$ are defined as

$$\boldsymbol{f}_{a,k+1}^{\text{int}} = \int_{\Omega_{FSI}} (\boldsymbol{P}_{k+1}^e + \boldsymbol{P}_{k+1}^v) \cdot \nabla N_a(\boldsymbol{x}) dV$$

$$= \sum_{p \in S(\boldsymbol{x}_{a,k})} \left(\boldsymbol{P}^e(\boldsymbol{F}_{p,k+1}) + \boldsymbol{P}^v(\dot{\boldsymbol{F}}_{p,k+1})\right) \cdot \nabla N_a(\boldsymbol{x}_{p,k}) w_{p,k}, \tag{43}$$
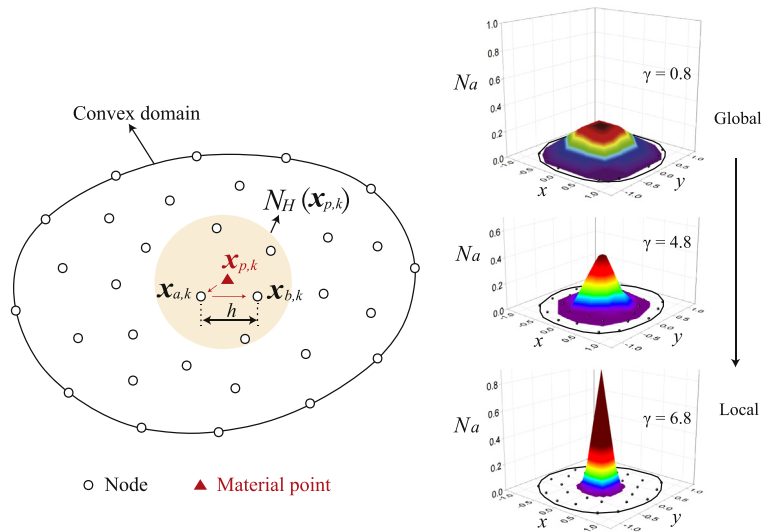
Fig. 2. The shape functions with different γ and the definition of local characteristic length h in a two-dimensional convex domain.

where $w_{p,k}$ is the volume of a material point $\boldsymbol{x}_{p,k}$ and $S(\boldsymbol{x}_{a,k})$ is the effective support range of node $\boldsymbol{x}_{a,k}$ at t_k. The external nodal forces $\boldsymbol{f}_{a,k+1}^{\text{ext}}$ are given by

$$
\begin{aligned}
\boldsymbol{f}_{a,k+1}^{\text{ext}} &= \int_{\Omega_{FSI}} \rho_k \boldsymbol{B}_{k+1} N_a(\boldsymbol{x}) dV + \int_{\Gamma_t} \overline{\boldsymbol{T}}_{k+1} N_a(\boldsymbol{x}) dA \\
&= \sum_{p \in S(\boldsymbol{x}_{a,k})} \rho_k \boldsymbol{B}(\boldsymbol{x}_{p,k}) N_a(\boldsymbol{x}_{p,k}) w_{p,k} + \sum_{q \in \gamma(\boldsymbol{x}_{a,k})} \overline{\boldsymbol{T}}(\theta_{q,k}) N_a(\theta_{q,k}) A_{q,k}.
\end{aligned}
\tag{44}
$$

Algorithm given in Table 1 outlines the general structure of the forward solution, which has the usual structure of explicit time-integration schemes, where the updated node coordinates are computed directly from the initial conditions at the beginning of the time step.

3.3. Fulid–Structure interface conditions

In the traditional partitioned approaches, the surface coupling between the fluid field and the structural field requires the transfer of fluid induced action force and displacement caused by structure on the Fluid–Structure interface (FS interface). In this paper, we employed a uniform set of governing equations in the Lagrangian description for both the fluid and solid subdomains. Additionally, we start with a conforming mesh for the entire domain with an explicit discretization of the FS interface. That ensures the nodes on the FS interface belonging to the fluid and solid simultaneously. As a consequence, the FS interface Γ_{FSI} (Fig. 3) becomes an internal surface that separates two different types of materials in the sense of continuum media. Therefore, the continuity condition of the FS interface is automatically satisfied, and dynamic tracking of the interface is a natural output of the Lagrangian framework without any extra computational cost, i.e.,

$$
\boldsymbol{u}_f(\boldsymbol{x}) \equiv \boldsymbol{u}_s(\boldsymbol{x}), \quad \forall \boldsymbol{x} \in \Gamma_{\text{FSI}}.
\tag{45}
$$

Meanwhile, the force equilibrium at the FS interface is guaranteed by the linear momentum conservation of the system. The fully discretized mechanical balance equation is reduced to the following form at the FS interface,

$$
\boldsymbol{f}_{a,k+1}^{\text{int}} = m_{a,k+1} \ddot{\boldsymbol{\varphi}}_{a,k+1}, \quad \forall \boldsymbol{x}_a \in \Gamma_{\text{FSI}}
\tag{46}
$$

where the right-hand side of the equation presents the inertia effect of the interface which competes with the internal forces generated by the fluid and solid domain. The definition of the internal nodal forces in Eq. (43) can be rewritten

Table 1
Spatial discretization algorithm.

Algorithm	Fluid-structure interaction
Step 1:	Set $k = 0$, initialize node coordinates $\boldsymbol{x}_{a,k}$, material point coordinates $\boldsymbol{x}_{p,k}$, volumes $w_{p,k}$, densities $\rho_{p,k}$, neighborhood $N_H(\boldsymbol{x}_{p,k})$, shape functions $N_a(\boldsymbol{x}_{p,k})$, shape function derivatives $\nabla N_a(\boldsymbol{x}_{p,k})$ and deformation gradient $\boldsymbol{F}_{p,k}$.
Step 2:	Compute mass matrix $\boldsymbol{M}_{a,k}$, linear momenta $\boldsymbol{l}_{a,k}$ and nodal forces $\boldsymbol{f}_{a,k}$.
Step 3:	Update node coordinates: $$\boldsymbol{x}_{a,k+1} = \boldsymbol{x}_{a,k} + (t_{k+1} - t_k)\boldsymbol{M}_{a,k}^{-1}\left(\boldsymbol{l}_{a,k} + \tfrac{t_{k+1}-t_{k-1}}{2}\boldsymbol{f}_{a,k}\right).$$
Step 4:	Compute material points incremental deformation gradients: $$\boldsymbol{F}_{p,k\rightarrow k+1} = \boldsymbol{x}_{a,k+1} \otimes \nabla N_a(\boldsymbol{x}_{p,k}).$$
Step 5:	Compute material points deformation gradients: $$\boldsymbol{F}_{p,k+1} = \boldsymbol{F}_{p,k\rightarrow k+1} \circ \boldsymbol{F}_{p,k}.$$
Step 6:	Update nodal forces: $\boldsymbol{f}_{a,k+1}^{int}$ and $\boldsymbol{f}_{a,k+1}^{ext}$.
Step 7:	Update linear momenta: $$\boldsymbol{l}_{a,k+1} = \boldsymbol{l}_{a,k} + \tfrac{1}{2}(\boldsymbol{f}_{a,k+1}) - \boldsymbol{f}_{a,k}(t_{k+1} - t_k).$$
Step 8:	Update mass matrix: $$\boldsymbol{M}_{a,k+1} = \sum_{p\in N_H(\boldsymbol{x}_{a,k})}m_p N_a(\boldsymbol{x}_{p,k}).$$
Step 9:	Update material point coordinates $\boldsymbol{x}_{p,k+1} = \sum_{a\in N_H(\boldsymbol{x}_{p,k})}\boldsymbol{x}_{a,k+1}N_a(\boldsymbol{x}_{p,k})$, neighborhood $N_H(\boldsymbol{x}_{p,k})$, volumes $w_{p,k+1} = \det(\boldsymbol{F}_{p,k\rightarrow k+1})w_{p,k}$ and densities $\rho_{p,k+1} = m_p/w_{p,k+1}$.
Step 10:	Recompute shape functions $N_a(\boldsymbol{x}_{p,k+1})$ and derivatives $\nabla N_a(x_{p,k+1})$ from updated node set.
Step 11:	Reset $k \leftarrow k + 1$. If $k = n$ exit (where n is the last time step index). Otherwise go to step 2.

more specifically for an FSI problem,

$$\boldsymbol{f}_{a,k+1}^{int} = \int_{\Omega_s\cup\Omega_f}\boldsymbol{P}_{k+1}\cdot\nabla N_a dV = \int_{\Omega_s}\boldsymbol{P}_{k+1}\cdot\nabla N_a dV + \int_{\Omega_f}\boldsymbol{P}_{k+1}\cdot\nabla N_a dV$$

$$= \sum_{p\in S_s(\boldsymbol{x}_{a,k})}\boldsymbol{P}_{k+1}\cdot\nabla N_a(\boldsymbol{x}_{p,k})w_{p,k} + \sum_{p\in S_f(\boldsymbol{x}_{a,k})}\boldsymbol{P}_{k+1}\cdot\nabla N_a(\boldsymbol{x}_{p,k})w_{p,k} \quad (47)$$

$$= \boldsymbol{f}_{a,k+1}^{s} + \boldsymbol{f}_{a,k+1}^{f},$$

where

$$\begin{cases} S_s(\boldsymbol{x}_{a,k}) = N_H(\boldsymbol{x}_{a,k}) \cap \Omega_s, \\ S_f(\boldsymbol{x}_{a,k}) = N_H(\boldsymbol{x}_{a,k}) \cap \Omega_f \end{cases} \quad (48)$$

and $\boldsymbol{f}_{a,k+1}^{f}$ and $\boldsymbol{f}_{a,k+1}^{s}$ denote the traction fields on $\boldsymbol{x}_a$ induced by the structure and fluid, respectively. Here, the effective support range $S(\boldsymbol{x}_{a,k})$ is not only dependent on a geometric factor,

$$N_H(\boldsymbol{x}_{a,k}) = \{\|\theta_q - \boldsymbol{x}_{a,k}\| \le R_{a,k}, \theta_q \in M_p\}, \quad (49)$$

where $R_{a,k}$ is the dynamic scope of the neighborhood determined by the material points effective range and M_p is the material point set of the entire domain (fluid and solid), but also the material to which the node belongs. Schematically Fig. 3 illustrates the definition of effective support range for the different type of nodes, which is similar to the visibility condition in meshfree methods. For instance, $\boldsymbol{x}_a$ on the FS interface has its neighborhood identical to $N_H(\boldsymbol{x}_a)$ and covering both the fluid and solid domain, while the support of an interior node of Ω_s (or Ω_f) is confined within Ω_s (or Ω_f). Thus, the internal nodal forces of interfacial nodes are assembled from both the fluid and solid material points to simulate the interaction between the fluid and solid domain. In a static case, the traditional interface traction balance can be obtained as

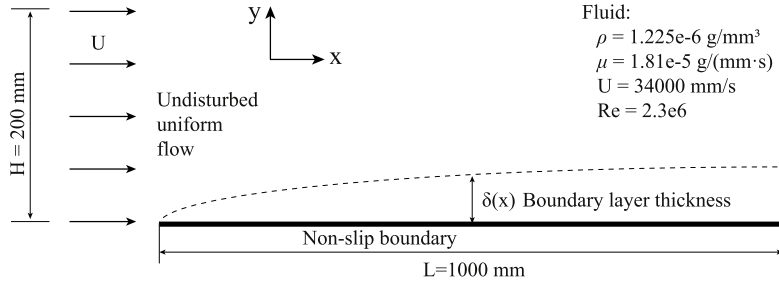$$\boldsymbol{f}_{a,k+1}^{s} = -\boldsymbol{f}_{a,k+1}^{f}. \quad (50)$$

Fig. 3. Schematic representation of FS interface in monolithic Lagrangian meshfree method.

4. Numerical tests and results

In this section, the accuracy and convergence characteristics of the OTM FSI approach are assessed by the classical Blasius solution of the boundary layer problem. In addition, the range and scope the method is demonstrated in two examples: the impact of a rigid body on the fluid domain in a container and the interaction between the fluid and highly flexible structures in an open channel.

4.1. Blasius solution

The Blasius boundary layer solution for flow over a flat plate is among the best known solutions in fluid mechanics. The boundary layer equations assume the following: steady, incompressible flow, laminar flow, no significant gradients of pressure in the x-direction, and velocity gradients in the x-direction are small compared to velocity gradients in the y-direction. The simplified Navier–Stokes Equations based on these assumptions, known as the boundary layer equations, are given as (see Ref. [50]):

$$
\begin{cases}
\dfrac{\partial u}{\partial x} + \dfrac{\partial v}{\partial y} = 0, \\
u\dfrac{\partial u}{\partial x} + v\dfrac{\partial u}{\partial y} = \nu\dfrac{\partial^2 u}{\partial y^2},
\end{cases}
\tag{51}
$$

where u and v are the x and y components of the velocity, and ν is the kinematic viscosity of the fluid. In the Blasius solution, a non-dimensional position η (the so-called similarity variable) combines both the x and y position:

$$
\eta = \frac{y^*}{\sqrt{x^*}} = \frac{y/\sqrt{\nu L/U}}{\sqrt{x/L}} = y\sqrt{\frac{U}{\nu x}},
\tag{52}
$$

where x^* and y^* are non-dimensional coordinates, U is the free stream velocity, and L is an arbitrary length scale that cancels itself out. The non-dimensional velocities u^* and v^* are then functions of non-dimensional stream function f:

$$
\begin{cases}
u^* = \dfrac{u}{U} = f'(\eta), \\
v^* = \dfrac{v}{\nu U/x} = 0.5[\eta f'(\eta) - f(\eta)].
\end{cases}
\tag{53}
$$

A governing equation for f can be found by inserting Eqs. (52) and (53) into Eq. (51), obtains the Blasius equation

$$
2f''' + f f'' = 0,
\tag{54}
$$

Fig. 4. Schematic of the Blasius flow applied in simulation (not to scale).

where the boundary conditions are no-slip, no through flow at the wall, and $u = U$ as y approaches infinity. In non-dimensional variable, these become:

$$\begin{cases} u^*(y = 0) = 0 \Rightarrow f'(\eta = 0) = 0, \\ v^*(y = 0) = 0 \Rightarrow f(\eta = 0) = 0, \\ u^*(y \to \infty) = 1 \Rightarrow f'(\eta \to \infty) = 1. \end{cases} \tag{55}$$

The non-linear differential equation (54) appears to be simple but difficult to solve analytically. Nevertheless, the Blasius equation can be solved numerically with the desirable accuracy. Blasius [51] himself gave a solution in power series for a viscous fluid past an infinitesimally thick, semi-infinite flat plate. This problem is employed as a benchmark to systematically investigate the characteristics (including accuracy, robustness and convergence) of the presented method. Fig. 4 shows the schematic of the Blasius flow in our simulations. The fluid with a characteristic height $H = 200$ mm is moving at a constant velocity $U = 34{,}000$ mm/s in the x-direction in the half-space $x < 0$. A flat plate with characteristic length $L = 1000$ mm is placed along the half-plane $y = 0$, $x > 0$ and modeled as a fixed solid domain. Thus, the fluid–structure interface is the fixed top surface of the flat plate, which is similar to no-slip boundary conditions to the fluid. The fluid density and viscosity are $\rho = 1.225$ kg/m^3 and $\mu = 1.81 \times 10^{-3}$ Pa s, respectively, which results in a high Reynolds number up to $Re = 2.3 \times 10^4$.

In our analysis, the normalized L_2 norm is used to quantify the difference between the numerical results and the theoretical considerations:

$$L2 = \left(\frac{\int_0^h \|u^h - u\|_2 dy}{\int_0^h \|u\|_2 dy} \right)^{\frac{1}{2}} = \left(\frac{\sum_{i=0} |u^h(y_i) - u(y_i)|^2 h_i}{\sum_{i=0} |u(y_i)|^2 h_i} \right)^{\frac{1}{2}}, \tag{56}$$

where $u^h(y_i)$ and $u(y_i)$ are the x components of the velocity at a position y_i calculated by numerical and the Blasius solution, respectively. Convergence study on the discretization size is conducted for $h = 4$ mm, 3 mm, 2 mm and 1 mm. In specific, the fluid domain is modeled by 402,802 degrees of freedom and 400,000 material points at $h = 1$ mm.

The results of the numerical investigations and comparisons are summarized in Figs. 5–7. It can be observed in Fig. 5 that a thin laminar boundary layer grows gradually till a stable status, while the flow velocity increases from zero at the wall to the incoming flow velocity U across the thickness of the boundary layer. The numerical values of the mean velocity profile as a function of the non-dimensional position η are compared with the Blasius solutions in Fig. 6. Particularly, the velocity field at locations $x = 500$ mm, 700 mm and 900 mm for a fine discretization of the domain converges to the analytical solution as the computation approaches to a steady state. Furthermore, the time evolution of the $L2$ error of the mean velocity field for various discretization sizes is shown from Figs. 7(a)–7(c). It can be observed that the accuracy of the numerical results at all the three locations is improved continuously with the refinement of the domain. A more detailed picture of the accuracy and convergence properties of the OTM FSI solution is afforded by conventional convergence plot, Fig. 7(d). The level of accuracy of the presented method revealed by our analysis is quite remarkable.
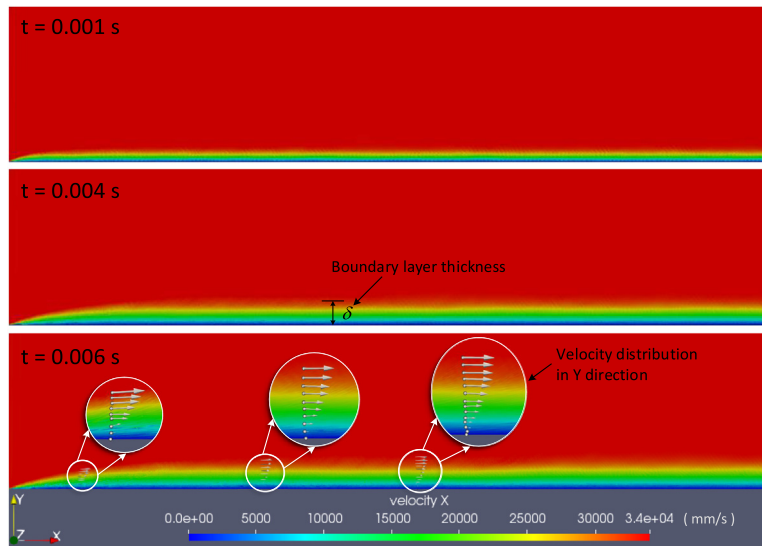
Fig. 5. Growth of a laminar boundary layer ($t = 0.006$ s) on the flat plate.

Table 2
Material and input parameters for the water impact tests.

Mass of wedge (g)	14.7694
Impact speed (mm/s)	1281
Water density (kg/m^3)	998
Shear viscosity of water (Pa s)	1.002×10^{-3}
Bulk modulus of water (Pa)	2.2×10^6
Tait-Murnaghan equation of state γ	7

4.2. Impact between fluid and rigid body

Aircraft crash landing on water is a complex FSI scenario, and conducting a large-scale test for aircraft water impact is expensive and also limited by test procedures and data measurement. Alternatively, numerical simulation is an enabling tool in ditching investigations for its low cost and high efficiency. [52,53]. In this section, a water impact of rigid wedge benchmark is performed, and the corresponding numerical results are compared to experimental measurements conducted by S. A. Shah et al. [54] to exhibit the capabilities of the OTM FSI approach.

The schematic of test facility and specimens are summarized in Fig. 8. Symmetric wedge impactors with various angles were dropped vertically into a water tank. To promote a two-dimensional fluid field upon impact, the length of the wedges was sized to give a 2 mm gap on each side of the water tank. The deadrise angle θ is defined between the horizontal and the wedge inclined face, as shown in Fig. 8(b). The wedges were manufactured from pinewood, sanded for consistency, and varnished to prevent water absorption. Also, sheet metal plates were added to ensure each wedge had the same mass. The impact event was filmed using a high-speed video camera at 500 frames/second and used to characterize the kinematic behavior of the impactor and fluid flow. Dots were drawn on the face of the wedge to generate the displacement-time history of the wedge. More experimental testing details can be found in Ref. [54].

In our numerical tests, models with a wedge depth of 3 mm were analyzed as shown in Fig. 8. The wedge was modeled as a rigid body with the density determined to match the experimental inertial characteristics of each wedge. Gravity with a gravitational acceleration equal to 5474 mm/s^2 was applied to the wedge due to the existence of friction of the test facility measured in experiments. Three deadrise angles ($\theta = 20°, 30°, 40°$, respectively) were tested. The water is modeled by 70,981 OTM nodes and 284,009 material points. The Tait–Murnaghan equation of state is employed to calculate the pressure in water. Table 2 lists the other parameters employed in the calculations.

Fig. 9 shows a qualitative comparison of the fluid flow patterns between the experiment and numerical predictions. It is evident that the time evolution of the deformed configuration of water along the wedge face is captured and
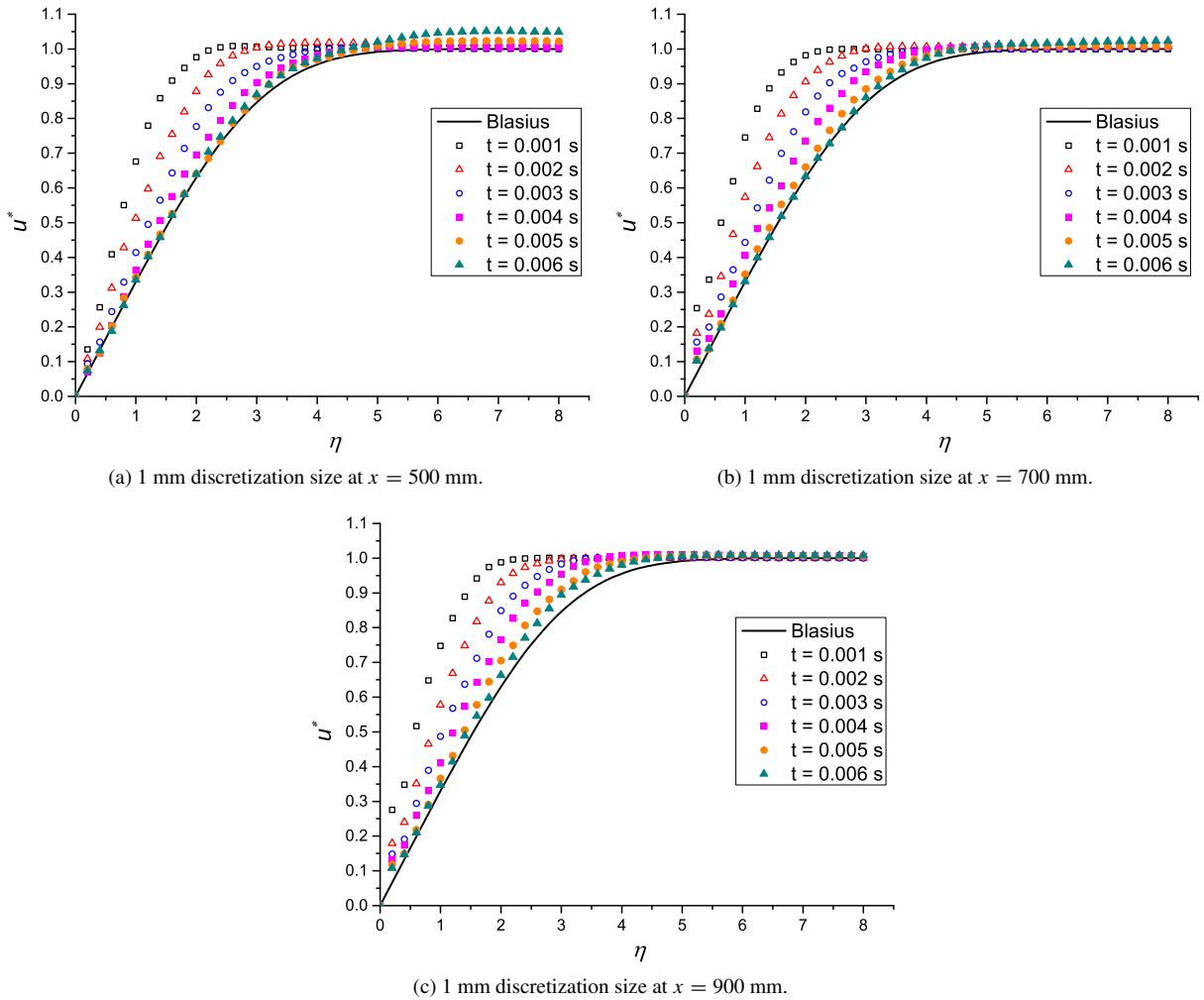
(a) 1 mm discretization size at $x = 500$ mm.

(b) 1 mm discretization size at $x = 700$ mm.

(c) 1 mm discretization size at $x = 900$ mm.

Fig. 6. Numerical results converge to the Blasius curve.

symmetric flow patterns can be observed along both sides of the wedge. In addition, the shape of the water crater and the depth of wedge penetration are in excellent agreement with experimental results. It is worth mentioning that, there were obvious *splash of water* phenomenon in experiments, while slightly *splash of material points* from the numerical results due to the resolution of the discretization. Fig. 10(a) and (b) demonstrate the effect of increasing deadrise angle on the force-time history and the maximum section force for each configuration, respectively. The wedge section force was determined by normalizing the wedge force by the depth. As shown in Fig. 10, the predicted impact forces are consistent with the experimental measurements. Furthermore, it is noteworthy that increasing the deadrise angle decreases the maximum impact force. This well-known phenomenon caused by low angle wedges producing a more bluff or slamming water entry [55] is successfully elucidated in the OTM FSI simulations.

4.3. Interaction between fluid and highly flexible structures

The last example concerns about the simulation of biological fluid flow interacting with highly deformable cells. Microfluidics is an attractive technology for the analysis and characterization of live erythrocytes (or Red Blood Cell, RBC) in physiological blood flows. However, several critical challenges in diagnostics and measurements have limited the application of microfluidic systems. In this study, microfluidic experiments were integrated with FSI simulations

(a) L2 vs. time steps ($x = 500$ mm).

(b) L2 vs. time steps ($x = 700$ mm).

(c) L2 vs. time steps ($x = 900$ mm).

(d) L2 vs. discretization size ($t = 0.06$ s).
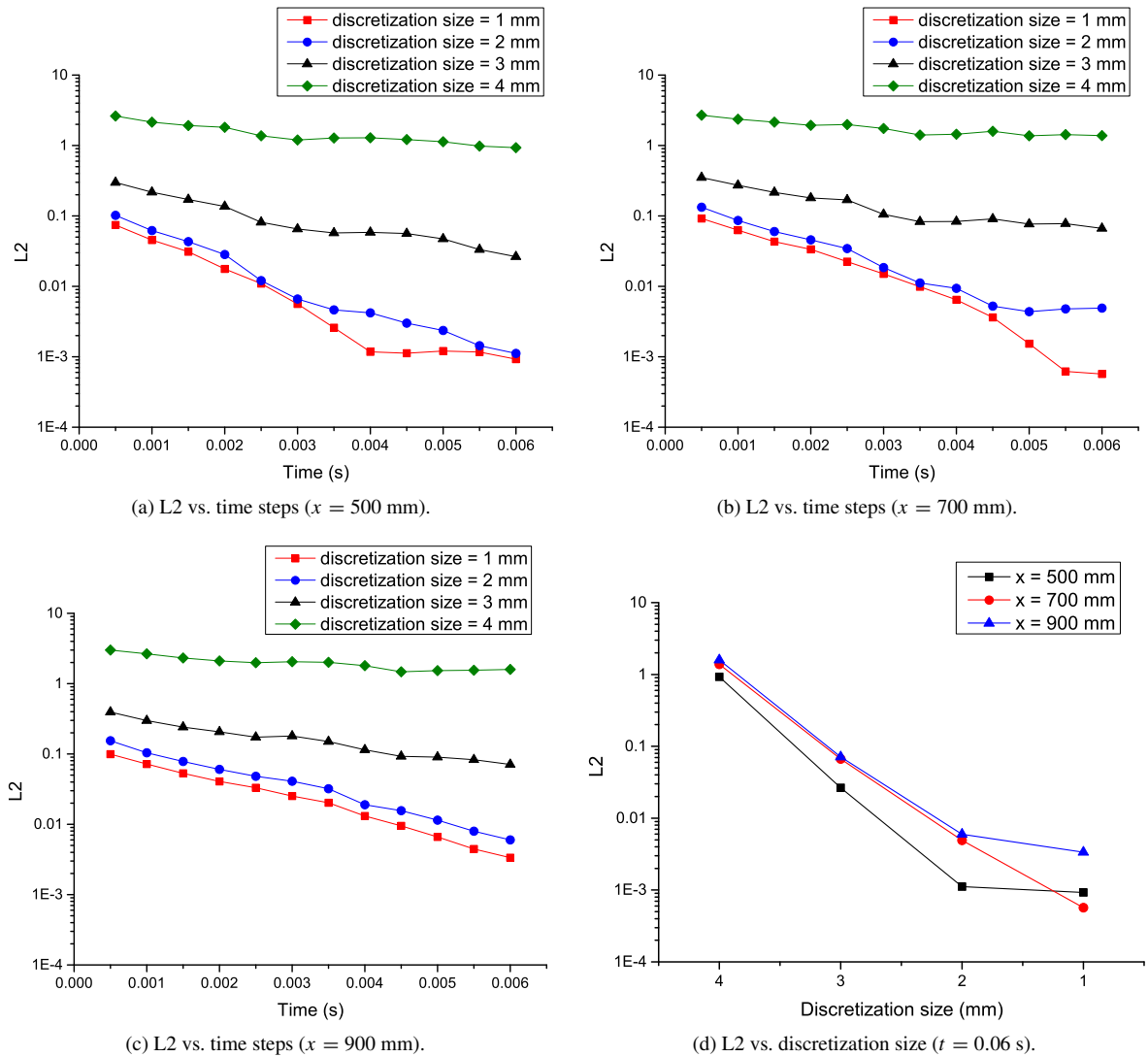
Fig. 7. The relationships among the $L2$ metric, time steps, and the discretization size.

to understand the cell dynamics under various flow rates and utilized to validate the computational framework as well. In the experiments, a 4 mm wide and 0.05 mm height micro-channel were fabricated by assembling a rectangular Poly (methyl methacrylate) (PMMA) piece onto glass with a microscope slide through a Double Sided Adhesive (DSA) film in between, while the specific immobilized endothelium protein (Laminin) was coated in the bottom surface of the channel as the substrate shown in Fig. 11(a). The prepared channels were placed horizontally on an inverted microscope stage (Olympus, IX 83) and the blood samples were perfused into the channels through a syringe pump at a constant volumetric flow rate that mimics blood flow in vessels. During experiments, after all the non-adhered cells were washed away, the flow rate was adjusted to produce different local flow velocities at cell adherent site, and the deformation of the adherent single cell was recorded until completely detached. The cell deformation was measured and represented by cell aspect ratio.

Meanwhile, three-dimensional simulations of the RBC in plasma were performed by the presented monolithic Lagrangian meshfree method. As sketched in Fig. 11(b) a cuboid with dimensions 180 μm × 24 μm × 12 μm in the vicinity of the cell is simulated. The RBC is modeled explicitly as a compound of RBC membrane and cytoplasm embedded in the plasma. Fig. 12 shows a cross-section of the discretization for the entire domain by a
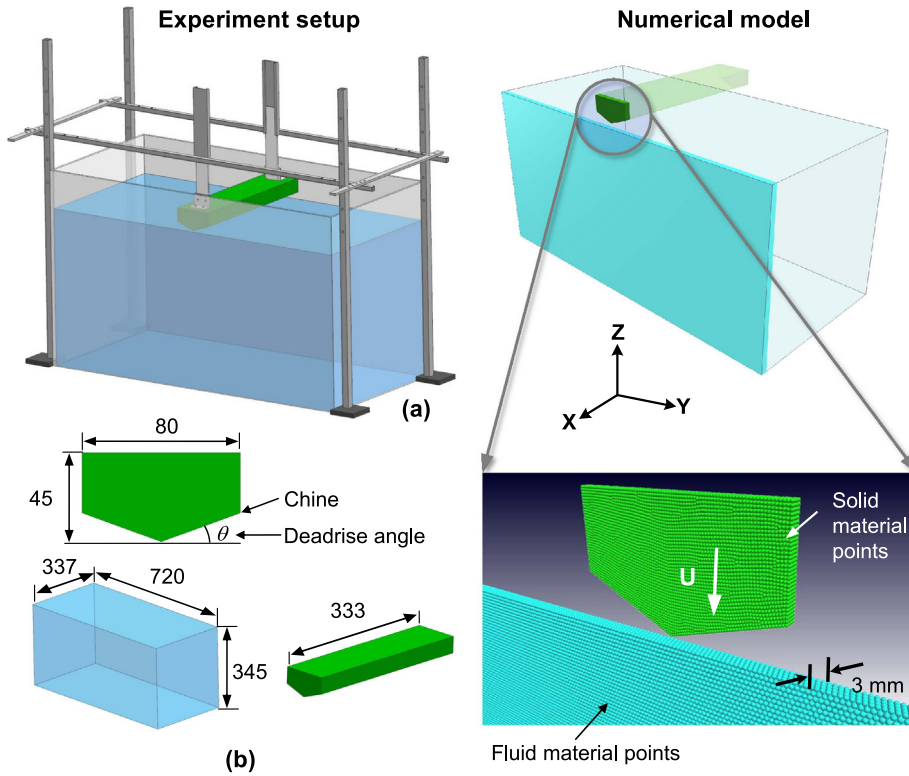
Fig. 8. Experiment setup [54]: (a) Test facility. (b) Wedge specimen dimensions (mm). Numerical model: the definition of numerical model applied in FSI simulation by the Monolithic Lagrangian Meshfree Method.

conforming tetrahedron mesh to initialize the position of the material points and nodes as well as the initial support. For simplicity, one material point is placed at the barycenter of each tetrahedron, and the vertices of the tetrahedron are selected as the initial neighborhood of the material point. Afterward, the connectivity list is completely jettisoned and not used anymore for a truly meshfree solution. While it is sufficient to use one integration point in the initial setup, it shows rank-deficiency instability as more nodes contribute to the material point at large deformations. To suppress the zero-energy modes, the stabilization algorithm proposed in [56,57] is implemented in the OTM method. In our computations, the initial velocity is uniform at a given local flow rate everywhere in the plasma, and the RBC (including the RBC membrane and cytoplasm) remains static. The boundary conditions are chosen as: slip boundary conditions at the top, bottom and sides of the plasma domain and do-nothing outflow boundary conditions at the end. The dynamic material point generation algorithm is employed to add plasma dynamically to the computational domain and maintain a constant incoming flow. The cytoplasm and plasma are modeled as nearly incompressible Newtonian fluid using the constitutive relation in Eq. (20) and the Tait–Murnaghan equation of state, where $K = 2 \times 10^7$ Pa is taken as their bulk modulus and $\gamma = 7$.

In addition, these simulations adopt the Mooney–Rivlin model presented by Skalak et al. for the nonlinear elastic response of the RBC membrane with the Helmholtz free energy density defined as $W(F) = \frac{C_1}{4}(\frac{1}{2}I_1^2 + I_1 - I_2) + \frac{C_2}{8}I_2^2$, where I_1 and I_2 are the first and second invariants of the right Cauchy–Green deformation tensor, respectively. Note that the viscoelastic response of RBCs commonly realized in literature is represented by the compound behavior of the membrane and cytoplasm in our model. Thus, one set of experiments for healthy RBCs at the flow rate of 1.454 mm/s was utilized to determine C_1 and C_2 by minimizing the difference between the predicted aspect ratio of the cell and the experimental data from a top view characterization using a Gradient-based optimization algorithm. The mean values of the shear modulus obtained from the calibration process are given by $C_1 = 2.3 \times 10^5$ Pa and $C_2 = 2.3 \times 10^4$ Pa. Fig. 13 shows a typical OTM simulation of the biological flow interacting with the highly deformable RBC.

In order to further validate the FSI algorithm, physical experiments and numerical simulations at various flow rates from 0.28 mm/s to 1.8 mm/s were conducted simultaneously. In all the calculations, the same shear modulus
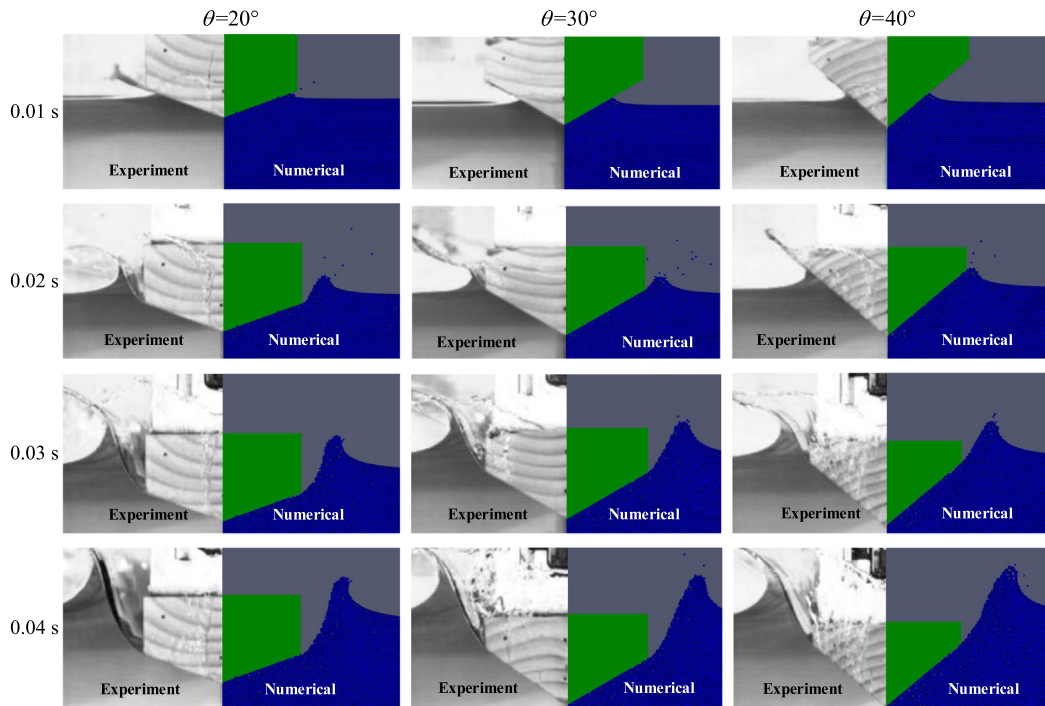
Fig. 9. The fluid flow patterns qualitative comparison between the experiment and numerical predictions with different deadrise angles θ at different time steps.
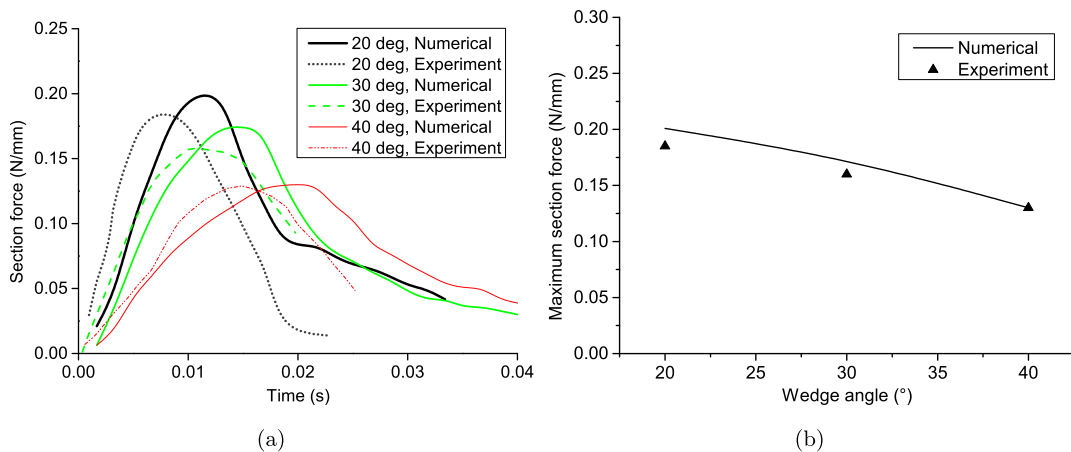

Fig. 10. (a) Section force time history comparison between the experiment and numerical predictions with varying deadrise angle, (b) Maximum section force comparison between the experiment and numerical predictions with varying deadrise angle.

obtained from calibration was used. Fig. 14 demonstrates the deformed configuration of the cell at steady state under different flow conditions as well as the maximum shear stress distribution in the membrane. A stress concentration on the cell is found near the adherent site and the concave shape of the RBC membrane due to the plasma-exerted drag forces and adhesive forces. In case that an adhesion model may be applied to the attachment site, the OTM FSI simulation furnishes an effective means of modeling the cell detachment process. Moreover, the stress concentration at the concave region, when the RBC is attached to the substrate, indicates a potential site for the rupturing of erythrocyte, also known as Hemolysis. A quantitative comparison of the predicted cell aspect ratio and the measured in experiments
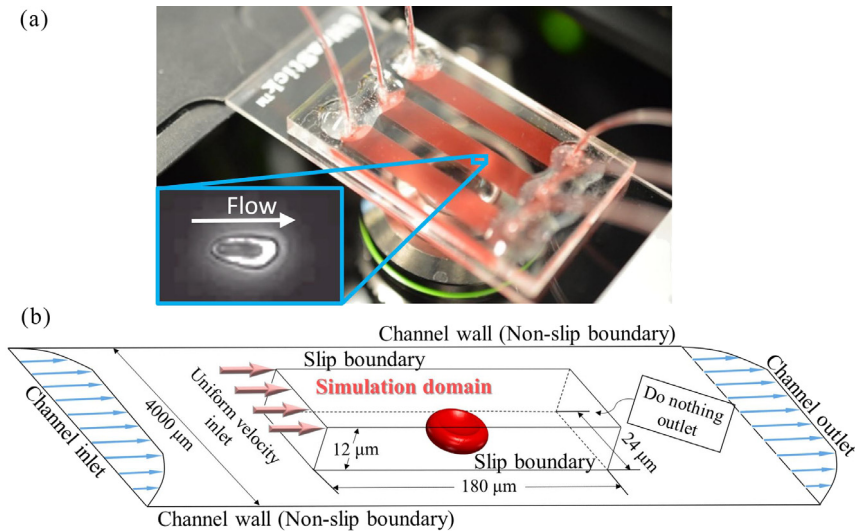
Fig. 11. The flow around single red blood cell. (a) The microfluidic device with the blood sample is placed on an inverted microscope. Snapshot of the individual adherent RBC under shear flow after channel washed is shown at the right corner. (b) The computational domain to analyze single cell dynamics.
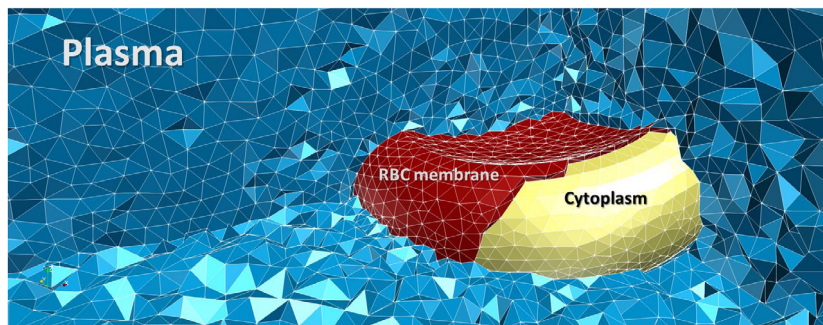

Fig. 12. Cross section of a typical conforming tetrahedron mesh for the entire computational domain.

is elucidated in Fig. 15. It is evident that the predicted shape of the healthy RBC (top view) is highly comparable with the deformed RBC shape imagined in real-time experiments. Furthermore, both the simulation and experimental data show the same trend regarding the non-linear change of cell aspect ratio with increasing local flow velocities. The predicted cell aspect ratio at various flow rates by the OTM FSI algorithm matches extraordinarily well the experimental data, which again implies the accuracy and robustness of the approach in modeling the fluid interacting with highly flexible structures.

5. Summary and conclusions

This paper presents a Monolithic Lagrangian Meshfree method for three dimensional Fluid–Structure Interaction (FSI) problems based on the Optimal Transportation Meshfree (OTM) framework. The governing equations for both fluid and structure domain are formulated in the Lagrangian configuration and solved simultaneously. In addition, a standard constitutive update algorithm is utilized to describe the dynamic responses of fluid and solid flows, based on which the variational formulation for general FSI problems with viscous dissipation mechanism is constructed. The corresponding fully-discretized variational formulation is obtained within the OTM framework. The time discretization furnished by optimal transportation theory for a general dissipative dynamic system leads to the formulation of robust and efficient state update algorithms and variational time integrator. Furthermore, the material
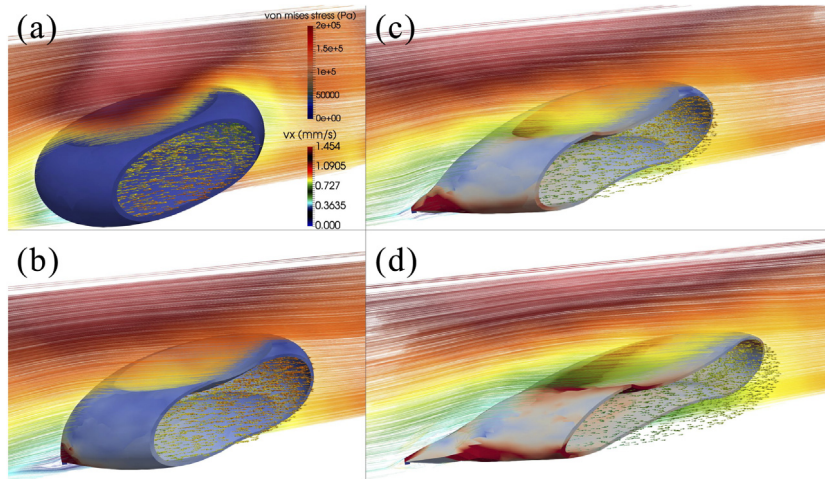
Fig. 13. Snapshots of the deformation of a red blood cell in plasma simulated by the OTM FSI algorithm at the flow rate of 1.454 mm/s. The membrane is represented by solid surface, the plasma by streamline and cytoplasm by velocity arrows. Color shows the von mises stress on the membrane and the velocity in the plasma and cytoplasm in the flow direction.
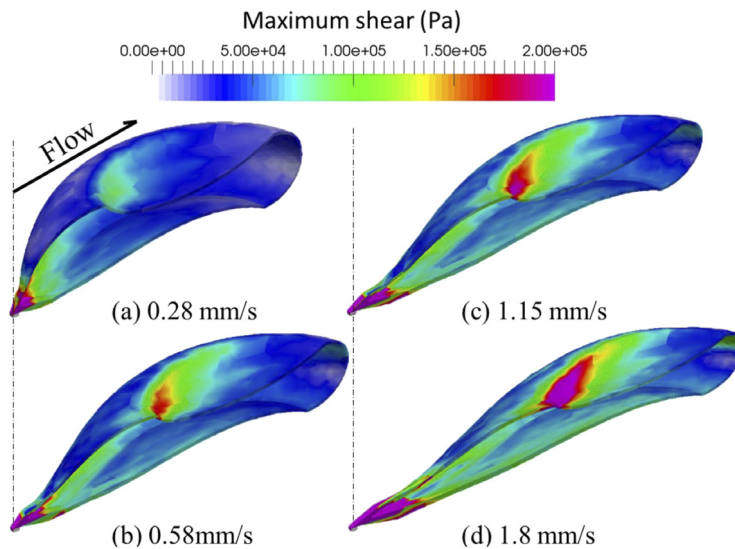

Fig. 14. The deformed configuration of RBCs at steady state predicted by the OTM FSI algorithm at various flow rate from 0.28 mm/s to 1.8 mm/s. The color scheme shows the maximum shear stress concentration on the RBC membrane.

point sampling is employed for a computationally convenient spatial discretization and numerical integration. The Local Maximum Entropy (LME) shape functions are adopted for approximating the incremental motion and fields requiring differentiation, which enables direct imposition of essential boundary conditions and strong coupling of fluid flows to highly deformable structures.

The proposed approach falls into the framework of monolithic Lagrangian FSI approaches and furnishes a Direct Numerical Simulation (DNS) of fluid flows. As a consequence, the fluid–structure interface becomes an internal surface of the coupled fluid–structure domain, and the continuity and force equilibrium is automatically satisfied without any extra computational cost. Furthermore, the use of Lagrangian formulations for fluid eliminates the problem of free surface and interface tracking and results in symmetric system matrices due to the absence of convective terms. The accuracy and robustness of the proposed approach are systematically investigated by the classical Blasius solution of the boundary layer problem. Furthermore, we illustrate the range and scope of the method
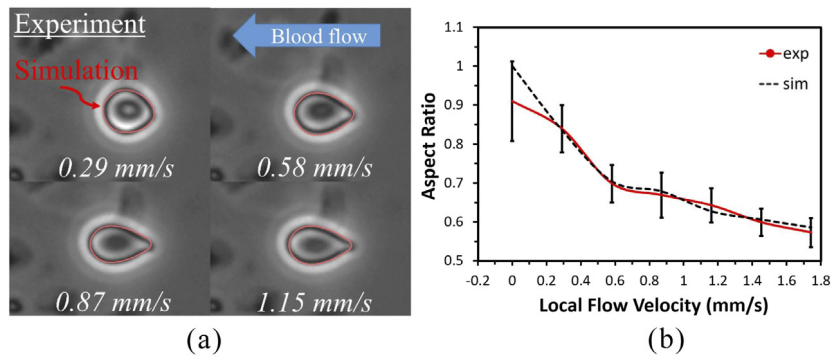
Fig. 15. Aspect ratio change of an adherent healthy RBC under different local flow velocities. (a) The predicted shape of the healthy RBC is comparable with the background real time experimental images. (b) Both the simulation and experimental data show the same trend regarding the non-linear change of cell aspect ratio with increasing local flow velocities.

using two examples of: the impact between the fluid and rigid body for closed systems, and the interaction between the fluid and highly flexible structure for open systems, in which we find excellent agreement between the numerical predictions and experimental measurements. The validation tests indicate that the proposed method possesses the potential for dealing with strongly coupled solid and fluid flows involving complex geometry, large deformation, general constitutive relations.

Acknowledgments

References

[1] G. Hou, J. Wang, A. Layton, Numerical methods for fluid–structure interaction—a review, Commun. Comput. Phys. 12 (2) (2012) 337–377.
[2] C.A. Felippa, K. Park, C. Farhat, Partitioned analysis of coupled mechanical systems, Comput. Methods Appl. Mech. Engrg. 190 (24–25) (2001) 3247–3270.
[3] C. Farhat, CFD-based Nonlinear Computational Aeroelasticity, in: Encyclopedia Comput. Mech., Wiley Online Library, 2004.
[4] R.A. Gingold, J.J. Monaghan, Smoothed particle hydrodynamics: theory and application to non-spherical stars, Mon. Not. R. Astron. Soc. 181 (3) (1977) 375–389.
[5] R. Gingold, J. Monaghan, Kernel estimates as a basis for general particle methods in hydrodynamics, J. Comput. Phys. 46 (3) (1982) 429–453.
[6] C. Farhat, M. Lesoinne, Two efficient staggered algorithms for the serial and parallel solution of three-dimensional nonlinear transient aeroelastic problems, Comput. Methods Appl. Mech. Engrg. 182 (3–4) (2000) 499–515.
[7] R.K. Jaiman, X. Jiao, P.H. Geubelle, E. Loth, Conservative load transfer along curved fluid–solid interface with non-matching meshes, J. Comput. Phys. 218 (1) (2006) 372–397.
[8] F. Nobile, Numerical Approximation of Fluid–structure Interaction Problems with Application to Haemodynamics, 2001, p. 203.
[9] P. Causin, J.-F. Gerbeau, F. Nobile, Added-mass effect in the design of partitioned algorithms for fluid–structure problems, Comput. Methods Appl. Mech. Engrg. 194 (42–44) (2005) 4506–4527.
[10] C. Förster, W.A. Wall, E. Ramm, Artificial added mass instabilities in sequential staggered coupling of nonlinear structures and incompressible viscous flows, Comput. Methods Appl. Mech. Engrg. 196 (7) (2007) 1278–1293.
[11] J. Degroote, P. Bruggeman, R. Haelterman, J. Vierendeels, Stability of a coupling technique for partitioned solvers in FSI applications, Comput. Struct. 86 (23–24) (2008) 2224–2234.
[12] J. Vierendeels, K. Dumont, E. Dick, P. Verdonck, Analysis and stabilization of fluid–structure interaction algorithm for rigid-body motion, AIAA J. 43 (12) (2005) 2549–2557.
[13] S. Osher, J.A. Sethian, Fronts propagating with curvature-dependent speed: algorithms based on Hamilton-Jacobi formulations, J. Comput. Phys. 79 (1) (1988) 12–49.
[14] J.M. Hyman, Numerical methods for tracking interfaces, Physica D 12 (1–3) (1984) 396–407.
[15] L. Li, S. Sherwin, P.W. Bearman, A moving frame of reference algorithm for fluid/structure interaction of rotating and translating bodies, Int. J. Numer. Meth. Fluid. 38 (2) (2002) 187–206.

[16] J. Kim, D. Kim, H. Choi, An immersed-boundary finite-volume method for simulations of flow in complex geometries, J. Comput. Phys. 171 (1) (2001) 132–150.

[17] J. Yang, S. Preidikman, E. Balaras, A strong coupling scheme for fluid–structure interaction problems in viscous incompressible flows, in: Proceedings of the International Conference on Computational Methods for Coupled Problems in Science and Engineering, 2005.

[18] M. Heil, An efficient solver for the fully coupled solution of large-displacement fluid–structure interaction problems, Comput. Methods Appl. Mech. Engrg. 193 (1–2) (2004) 1–23.

[19] K.J. Bathe, H. Zhang, Finite element developments for general fluid flows with structural interactions, Internat. J. Numer. Methods Engrg. 60 (1) (2004) 213–232.

[20] J. Hron, S. Turek, A monolithic FEM/multigrid solver for an ALE formulation of fluid–structure interaction with applications in biomechanics, in: Fluid–structure Interaction, Springer, 2006, pp. 146–170.

[21] C. Michler, S. Hulshoff, E. Van Brummelen, R. De Borst, A monolithic approach to fluid–structure interaction, Comput. & Fluids 33 (5–6) (2004) 839–848.

[22] J. Donea, S. Giuliani, J.-P. Halleux, An arbitrary Lagrangian-Eulerian finite element method for transient dynamic fluid–structure interactions, Comput. Methods Appl. Mech. Engrg. 33 (1–3) (1982) 689–723.

[23] J. Donea, A. Huerta, J.P. Ponthot, A. Rodriguez-Ferran, Arbitrary Lagrangian ulerian methods, in: Encyclopedia Comput. Mech., John Wiley & Sons, 2004, pp. 413–437.

[24] T.J. Hughes, W.K. Liu, T.K. Zimmermann, Lagrangian-Eulerian finite element formulation for incompressible viscous flows, Comput. Methods Appl. Mech. Engrg. 29 (3) (1981) 329–349.

[25] J. Donea, A. Huerta, Finite Element Methods for Flow Problems, John Wiley & Sons, 2003.

[26] S.R. Idelsohn, F. Del Pin, R. Rossi, E. Oñate, Fluid–structure interaction problems with strong added-mass effect, Internat. J. Numer. Methods Engrg. 80 (10) (2009) 1261–1294.

[27] R. Rossi, E. Oñate, Analysis of some partitioned algorithms for fluid–structure interaction, Eng. Comput. 27 (1) (2010) 20–56.

[28] T.E. Tezduyar, M. Behr, J. Liou, A new strategy for finite element computations involving moving boundaries and interfaces - The deforming-spatial-domain/space-time procedure: I. The concept and the preliminary numerical tests, Comput. Methods Appl. Mech. Engrg. 94 (3) (1992) 339–351.

[29] T.E. Tezduyar, M. Behr, S. Mittal, J. Liou, A new strategy for finite element computations involving moving boundaries and interfaces–the deforming-spatial-domain/space-time procedure: II. Computation of free-surface flows, two-liquid flows, and flows with drifting cylinders, Comput. Methods Appl. Mech. Engrg. 94 (3) (1992) 353–371.

[30] S. Mittal, T.E. Tezduyar, Parallel finite element simulation of 3D incompressible flows: Fluid–structure interactions, Int. J. Numer. Meth. Fluid. 21 (10) (1995) 933–953.

[31] T.E. Tezduyar, S. Sathe, R. Keedy, K. Stein, Space–time finite element techniques for computation of fluid–structure interactions, Comput. Methods Appl. Mech. Engrg. 195 (17–18) (2006) 2002–2027.

[32] T.E. Tezduyar, S. Sathe, Modelling of fluid–structure interactions with the space–time finite elements: solution techniques, Int. J. Numer. Meth. Fluid. 54 (6–8) (2007) 855–900.

[33] Y. Bazilevs, V.M. Calo, T.J. Hughes, Y. Zhang, Isogeometric fluid–structure interaction: theory, algorithms, and computations, Comput. Mech. 43 (1) (2008) 3–37.

[34] S.R. Idelsohn, J. Marti, A. Limache, E. Oñate, Unified Lagrangian formulation for elastic solids and incompressible fluids: application to fluid–structure interaction problems via the PFEM, Comput. Methods Appl. Mech. Engrg. 197 (19–20) (2008) 1762–1776.

[35] E. Oñate, S.R. Idelsohn, F. Del Pin, R. Aubry, The particle finite element method—an overview, Int. J. Comput. Meth. 1 (02) (2004) 267–307.

[36] S.R. Idelsohn, E. Oñate, F. Del Pin, N. Calvo, Fluid–structure interaction using the particle finite element method, Comput. Methods Appl. Mech. Engrg. 195 (17–18) (2006) 2100–2123.

[37] B. Li, F. Habbal, M. Ortiz, Optimal transportation meshfree approximation schemes for fluid and plastic flows, Internat. J. Numer. Methods Engrg. 83 (12) (2010).

[38] B. Li, A. Kidane, G. Ravichandran, M. Ortiz, Verification and validation of the optimal transportation meshfree (otm) simulation of terminal ballistics, Int. J. Imp. Eng. 42 (2012) 25–36.

[39] C. Villani, Topics in Optimal Transportation, vol. 58, American Mathematical Soc., 2003.

[40] M. Arroyo, M. Ortiz, Local maximum-entropy approximation schemes: a seamless bridge between finite elements and meshfree methods, Internat. J. Numer. Methods Engrg. 65 (13) (2006) 2167–2202.

[41] D. Sulsky, Z. Chen, H.L. Schreyer, A particle method for history-dependent materials, Comput. Methods Appl. Mech. Engrg. 118 (1–2) (1994) 179–196.

[42] R. Radovitzky, M. Ortiz, Lagrangian finite element analysis of Newtonian fluid flows, Internat. J. Numer. Methods Engrg. 43 (4) (1998) 607–619.

[43] R. Radovitzky, M. Ortiz, Error estimation and adaptive meshing in strongly nonlinear dynamic problems, Comput. Methods Appl. Mech. Engrg. 172 (1–4) (1999) 203–240.

[44] J Ross Macdonald, Some simple isothermal equations of state, Rev. Modern Phys. 38 (4) (1966) 669.

[45] M. Ortiz, L. Stainier, The variational formulation of viscoplastic constitutive updates, Comput. Methods Appl. Mech. Engrg. 171 (3–4) (1999) 419–444.

[46] Q. Yang, L. Stainier, M. Ortiz, A variational formulation of the coupled thermo-mechanical boundary-value problem for general dissipative solids, J. Mech. Phys. Solids 54 (2) (2006) 401–424.

[47] J.-D. Benamou, Y. Brenier, A numerical method for the optimal time-continuous mass transport problem and related problems, Contemp. Math. 226 (1999) 1–12.

[48] J.-D. Benamou, Y. Brenier, A computational fluid mechanics solution to the Monge-Kantorovich mass transfer problem, Numer. Math. 84 (3) (2000) 375–393.

[49] R.J. McCann, A convexity principle for interacting gases, Adv. Math. 128 (1) (1997) 153–179.

[50] M.J. Martin, I.D. Boyd, Blasius boundary layer solution with slip flow conditions, AIP Conf. Proc. 585 (1) (2001) 518–523.

[51] H. Blasius, Grenzschichten in Flüssigkeiten mit kleiner Reibung, Druck von BG Teubner, 1907.

[52] N. Pentecôte, A. Vigliotti, Crashworthiness of helicopters on water: Test and simulation of a full-scale WG30 impacting on water, Int. J. Crashworth. 8 (6) (2003) 559–572.

[53] M. Anghileri, L.-M.L. Castelletti, E. Francesconi, A. Milanese, M. Pittofrati, Rigid body water impact–experimental tests and numerical simulations using the sph method, Int. J. Imp. Eng. 38 (4) (2011) 141–151.

[54] S. Shah, A. Orifici, J. Watmuff, Water impact of rigid wedges in two-dimensional fluid flow, J. Appl. Fluid Mech. 8 (2) (2015) 329–338.

[55] S.-L. Chuang, Slamming of Rigid Wedge-shaped Bodies with Various Deadrise Angles, David Taylor Model Basin Washington DC Structural Mechanics Lab, 1966.

[56] G.C. Ganzenmuller, An hourglass control algorithm for Lagrangian smooth particle hydrodynamics, Comput. Methods Appl. Mech. Engrg. (ISSN: 0045-7825) 286 (2015) 87–106.

[57] C. Weisenfels, P. Wriggers, Stabilization algorithm for the optimal transportation meshfree approximation scheme, Comput. Methods Appl. Mech. Engrg. (ISSN: 0045-7825) 329 (2018) 421–443.